NeuroImage 230 (2021) 117793

Contents lists available at ScienceDirect

NeuroImage

journal homepage: www.elsevier.com/locate/neuroimage

Localization accuracy of a common beamformer for the comparison of two conditions

Gustavo Lucena Gómez[a,*], Philippe Peigneux[b], Vincent Wens[a,c,1], Mathieu Bourguignon[a,d,e,1]

[a] Laboratoire de Cartographie fonctionnelle du Cerveau, UNI – ULB Neuroscience Institute, Université libre de Bruxelles (ULB), Brussels, Belgium
[b] UR2NF – Neuropsychology and Functional Neuroimaging Research Unit at CRCN – Centre de Recherches Cognition et Neurosciences, and UNI – ULB Neuroscience Institute, Université libre de Bruxelles (ULB), Brussels, Belgium
[c] Magnetoencephalography unit, Department of Functional Neuroimaging, Service of Nuclear Medicine, CUB Hôpital Erasme, Brussels, Belgium
[d] BCBL, Basque Center on Cognition, Brain and Language, 20009 San Sebastian, Spain
[e] Laboratoire Cognition Langage et Développement, UNI – ULB Neuroscience Institute, Université libre de Bruxelles (ULB), Brussels, Belgium

ARTICLE INFO

Keywords:
Beamformer
Functional mapping
Magnetoencephalography
Linearly constrained minimum variance
Source estimation

ABSTRACT

The linearly constrained minimum variance beamformer is frequently used to reconstruct sources underpinning neuromagnetic recordings. When reconstructions must be compared across conditions, it is considered good practice to use a single, "common" beamformer estimated from all the data at once. This is to ensure that differences between conditions are not ascribable to differences in beamformer weights. Here, we investigate the localization accuracy of such a common beamformer. Based on theoretical derivations, we first show that the common beamformer leads to localization errors in source reconstruction. We then turn to simulations in which we attempt to reconstruct a (genuine) source in a first condition, while considering a second condition in which there is an (interfering) source elsewhere in the brain. We estimate maps of mislocalization and assess statistically the difference between "standard" and "common" beamformers. We complement our findings with an application to experimental MEG data. The results show that the common beamformer may yield significant mislocalization. Specifically, the common beamformer may force the genuine source to be reconstructed closer to the interfering source than it really is. As the same applies to the reconstruction of the interfering source, both sources are pulled closer together than they are. This observation was further illustrated in experimental data. Thus, although the common beamformer allows for the comparison of conditions, in some circumstances it introduces localization inaccuracies. We recommend alternative approaches to the general problem of comparing conditions.

1. Introduction

Magnetoencephalography (MEG) is a functional brain imaging technique that measures the scalp magnetic field resulting from the electrical currents flowing through the apical dendrites of neurons (Hämäläinen et al., 1993). This technique is appreciated for being non-invasive and for having outstanding temporal resolution (of the order of the millisecond) (Hari and Puce, 2017). It also features a good spatial resolution (of the order of 5 mm) for focal cortical sources. However, reconstructing the electrical current distribution from MEG data is an ill-posed inverse problem (Hämäläinen et al., 1993). For example, such a problem admits more than one solution, as there exist source configurations in the brain that produce no extracranial magnetic field. One therefore needs to add constraints, which lead to several types of source reconstruction methods.

One of the most widely used source reconstruction methods is the linearly constrained minimum variance (LCMV) beamformer (Hillebrand et al., 2005; Robinson, 1999; vanVeen et al., 1997). In the present work we will refer to this filter simply as the *beamformer*. It is a linear spatial filter, meaning that it estimates the source activity at a given brain location as a weighted sum of the MEG data at different sensors. By successively scanning over a source grid covering the entire brain, one can build maps of brain activity. The beamformer is also adaptive, which means that its weights depend on the measured MEG data via their covariance matrix (Sekihara and Nagarajan, 2008). This dependence gives to the beamformer one of its most interesting properties: it reconstructs activity from scanned sources while suppressing interferences (from remote sources or undesirable artifacts) without having to specify their configuration (Hillebrand et al., 2005; Robinson, 1999; vanVeen et al., 1997). Another desirable property of the beamformer is that it exhibits no mislocalization, at least with suitable depth bias correction and when

* Corresponding author.
E-mail address: glucenag@gmail.com (G. Lucena Gómez).
[1] These authors equally contributed to the article.

https://doi.org/10.1016/j.neuroimage.2021.117793
Received 25 May 2020; Received in revised form 3 November 2020; Accepted 15 January 2021
Available online 23 January 2021

sensor noise is homogeneous without any cross-talk (Greenblatt et al., 2005).

In some cases however, the beamformer leads to confusing results. This occurs specifically when reconstructed source maps are compared between conditions, precisely because the beamformer is adaptive. Differences between source maps reconstructed with the beamformer can stem from a difference in the beamformer weights rather than in brain activity *per se*. To circumvent this ambiguity, a workaround was proposed as good practice (Gross et al., 2013). The idea is to apply to both conditions a *common* beamformer based on the covariance matrix averaged over the two conditions. Since the filter weights are now identical, differences between source maps can be securely ascribed to differences between conditions.

To the best of our knowledge, the adequacy of such a common beamformer and in particular its localization accuracy, has not yet been assessed. In fact, since it implies estimating the filter's weights from a covariance matrix that does not correspond to the underlying source configuration, it is legitimate to expect some amount of mislocalization (Greenblatt et al., 2005). In the present report, we appraise the localization accuracy of the common beamformer in simple situations in which two conditions are associated with single sources with variable inter-source distance and signal-to-noise ratio (SNR). We first demonstrate analytically the existence of mislocalization (see Section 2) and quantify it on realistic simulations as well as on experimental MEG data (see Sections 3 and 4).

2. Theory

In the present section, we explore analytically the localization accuracy of the common beamformer. The following considerations focus on the estimation of one-dimensional dipolar sources and homogeneous, diagonal measurement noise, as in Sekihara and Nagarajan (2008). However the derived insights hold more generally, as will be illustrated in Section 4.

2.1. General setting

A unit current dipole at location $\vec{r}$ generates a topographical distribution of sensor response known as the source gain and represented here as a column vector $g = g(\vec{r})$. Using the beamformer with unit-noise-gain constraint (Sekihara and Nagarajan, 2008), a given sensor topography b is mapped onto a source distribution $s(\vec{r}) = w(\vec{r})b$ via the weights

$$w(\vec{r}) = \frac{g(\vec{r})^{\mathrm{T}}\Sigma^{-1}}{\sqrt{g(\vec{r})^{\mathrm{T}}\Sigma^{-2}g(\vec{r})}}\,, \tag{1}$$

with Σ a sensor data covariance matrix whose choice is the topic of the present paper. We have chosen here the unit-noise-gain normalization $||w(\vec{r})|| = 1$ to ensure the absence of localization biases when Σ corresponds to the data b (Greenblatt et al., 2005).

We consider a simple situation where a single dipolar source is active in two separate conditions. In condition 1, this source is located at $\vec{r}_1$ and its time course has zero mean and standard deviation σ_1. In condition 2, the source is moved at another location $\vec{r}_2$ and its time course has zero mean and standard deviation σ_2. The corresponding data covariance matrices are

$$\Sigma_1 = \sigma_1^2 g_1 g_1^{\mathrm{T}} + \sigma_0^2 \mathbb{I} \qquad \text{and} \qquad \Sigma_2 = \sigma_2^2 g_2 g_2^{\mathrm{T}} + \sigma_0^2 \mathbb{I}\,, \tag{2}$$

where $g_1 = g(\vec{r}_1)$ and $g_2 = g(\vec{r}_2)$ denote the gain at the two source locations. These covariance matrices also contain the independent contribution of diagonal sensor noise with variance σ_0^2 at each sensor. In the standard beamformer formulation, Σ in formula (1) is Σ_1 in condition 1 and Σ_2 in condition 2. The common beamformer approach rather prescribes using the average

$$\Sigma = \frac{1}{2}(\Sigma_1 + \Sigma_2)\,. \tag{3}$$

Without loss of generality, we will only focus on the source reconstruction for condition 1. Accordingly, the source active in condition 1 will be called the *genuine* source, and the source active in condition 2 the *interfering* source. The combination (3) of the two single-source activation models (2) is mathematically equivalent to a fictitious common condition containing these two sources simultaneously active (with standard deviation diminished by a factor $\sqrt{2}$) and temporally uncorrelated. Our goal is to investigate how the inclusion of the source in condition 2 interferes with the reconstruction of the source in condition 1, hence our terminology. However, it is important to emphasize that the two sources are never active at the same time as they are present in separate conditions. Introducing a temporal correlation between them would not reflect the problem at hand.

2.2. Analytical considerations

The basic tool to investigate localization accuracy is the point-spread function

$$F_1(\vec{r}) = w(\vec{r})g_1 \tag{4}$$

of the genuine source. It represents the source distribution estimated by the beamformer (1) when it is applied to a sensor distribution generated by a unit source at $\vec{r}_1$ in the absence of noise. It can also be viewed as the square root of the beamformer output power, $P_1(\vec{r}) = F_1(\vec{r})^2$. Using the point-spread function F_1 turns out to be more convenient for analytical developments and we follow this convention below. However, when turning to simulated and experimental data in Sections 3 and 4, we shall switch to the power formulation. With an unbiased beamformer, the global maximum of $F_1(\vec{r})$ occurs at $\vec{r}_1$ (Sekihara and Nagarajan, 2008). Mislocalization is thus defined as the difference in location between the global maximum of $F_1(\vec{r})$ and $\vec{r}_1$. Under the assumption that measurement noise is diagonal and of equal variance for each sensor, we derive the analytic form of F_1 in the supplementary material S1. The profile of F_1 depends on the source standard deviations σ_i $(i = 1, 2)$ in the two conditions through the SNR parameters

$$\alpha_i = \frac{\sigma_i^2}{\sigma_0^2}\,||g_i||^2\,, \quad i = 1, 2\,, \tag{5}$$

and on the angles between the gain vectors $g(\vec{r})$, g_1, and g_2 (which measure the overlap of their sensor-level topographies due to magnetic field spread).

An adaptation of the localization argument in Sekihara and Nagarajan (2008) can be used to show that F_1 reaches its global maximum at location $\vec{r}$ if $g(\vec{r})$ is proportional to

$$g_{\mathrm{MAX}} = (2 + \alpha_1)\,\hat{g}_1 + \alpha_2 \cos(\theta_{12})\,\hat{g}_2\,, \tag{6}$$

where $\hat{g}_i$ $(i = 1, 2)$ is the gain vector g_i rescaled to have unit norm and θ_{12} is the angle between g_1 and g_2 $(\cos(\theta_{12}) = \hat{g}_1^{\mathrm{T}}\hat{g}_2)$. The proof is developed in the supplementary material S1. The sensor topography (6) is a linear mixture of the two gain vectors weighted by their SNR and overlap. Strictly speaking, it does not correspond to any dipolar topography $g(\vec{r})$ because a single current dipole cannot produce exactly the distribution generated by two separate non-silent dipoles. So this criterion to locate the global maximum does not apply, except when: (i) there is no interfering source $(\alpha_2 = 0)$, which reduces to the standard beamformer, (ii) the genuine and interfering sources generate similar sensor topographies (g_1 and g_2 are proportional; $\hat{g}_1 = \pm\hat{g}_2$ and $\cos(\theta_{12}) = \pm 1$), which generically occurs only when they co-localize $(\vec{r}_1 = \vec{r}_2)$, and (iii) their sensor topographies do not overlap (g_1 and g_2 are orthogonal; $\cos(\theta_{12}) = 0$), which corresponds to situations where genuine and interfering sources are very far apart or in a very different orientation. In these situations, the common beamformer localizes accurately at $\vec{r} = \vec{r}_1$ since g_{MAX} is proportional to g_1. The cases of interest (ii) and (iii) show that mislocalization can only occur for interfering sources within a shell around the genuine source, neither too close nor too far away.

In this in-between situation, the above criterion cannot locate strictly the global maximum but it can nevertheless provide an approximation, as there might exist a dipole location $\vec{r}_B$ (that will be dubbed *best fitting*) for which the gain vector $g_B = g(\vec{r}_B)$ resembles the topography g_{MAX}. This occurs when the genuine and interfering sources are nearby. In fact, we show in the supplementary material S1 that $g_{MAX} \approx g(\vec{r}_B)$ (up to an irrelevant renormalization of g_{MAX} and up to quadratic corrections in $||\vec{r}_2 - \vec{r}_1||$), where

$$\vec{r}_B \approx (1-\rho)\vec{r}_1 + \rho\vec{r}_2 \quad \text{with} \quad \rho = \frac{\alpha_2 \cos(\theta_{12})||g_1||/||g_2||}{2+\alpha_1+\alpha_2\cos(\theta_{12})||g_1||/||g_2||}\,. \tag{7}$$

Furthermore, within this approximation we may expect the global maximum of the point-spread function F_1 to localize closer to $\vec{r}_B$ than to the genuine source location $\vec{r}_1$. This means that, when the genuine and interfering sources are not too distant, the common beamformer will mislocalize the genuine source somewhere in between $\vec{r}_1$ and $\vec{r}_2$. Note, however, that the best-fitting location $\vec{r}_B$ does not necessarily coincide with the global maximum of the beamformer output, so Eq. (7) should not be used to quantify localization errors. In fact, mislocalization actually occurs between $\vec{r}_1$ and $\vec{r}_B$, as we discuss now.

To better characterize this mislocalization, let us consider the explicit expression of the filter weights $w(\vec{r})$ and the associated point-spread function $F_1(\vec{r})$. In the nearby-source approximation (7) where g_1 and g_2 both closely resemble $g(\vec{r}_B) = g_B$, the common beamformer reduces to a standard beamformer associated with the best-fitting dipolar source with equivalent standard deviation $\sigma_B = \sqrt{(\sigma_1^2+\sigma_2^2)/2}$, so

$$w(\vec{r}) \approx \frac{\hat{g}(\vec{r})^T - a_B(\hat{g}(\vec{r})^T\hat{g}_B)\hat{g}_B^T}{\sqrt{1-b_B(\hat{g}(\vec{r})^T\hat{g}_B)^2}}\,, \tag{8}$$

with $a_B = \alpha_B/(\alpha_B+2)$, $b_B = \alpha_B(\alpha_B+4)/(\alpha_B+2)^2$, and $\alpha_B = \sigma_B^2||g_B||^2/\sigma_0^2$. We show in the supplementary material S1 that this holds up to quadratic corrections in $||\vec{r}_2 - \vec{r}_1||$ and at sufficiently large equivalent SNR, $\alpha_B \gg 1$ (so here $a_B \approx b_B \approx 1$). This analytic form can be understood from the basic optimization problem defining the beamformer (Sekihara and Nagarajan, 2008). The first term in the numerator is proportional to the gain pattern $\hat{g}(\vec{r})$ due to the unit-gain constraint. The second reflects the suppression of the equivalent source activity at $\vec{r}_B$ (which approximately combines the suppression of the genuine and interfering sources) due to variance minimization. The denominator merely enforces the unit-noise-gain normalization. Since the weights are tuned to suppress activity from $\vec{r}_B$ rather than $\vec{r}_1$, the corresponding point-spread function (4)

$$F_1(\vec{r}) \approx ||g_1||\frac{(\hat{g}(\vec{r})^T\hat{g}_1) - a_B(\hat{g}_B^T\hat{g}_1)(\hat{g}(\vec{r})^T\hat{g}_B)}{\sqrt{1-b_B(\hat{g}(\vec{r})^T\hat{g}_B)^2}} \tag{9}$$

exhibits a competition between (i) the profile of topographical overlap of the genuine source $(\hat{g}(\vec{r})^T\hat{g}_1)$, which peaks at $\vec{r}_1$, and (ii) that of the best-fitting source $(\hat{g}(\vec{r})^T\hat{g}_B)$, which peaks at $\vec{r}_B$. The second term in the numerator and the denominator (both driven by the combined suppression of the genuine and interfering sources) will conspire to move the global maximum away from $\vec{r}_1$ towards $\vec{r}_B$, so mislocalization emerges in between $\vec{r}_1$ and $\vec{r}_B$. The best-fitting dipole location thus acts as an "attractor" for the global maximum. This is illustrated by the fact that the point-spread function may reach higher values at $\vec{r}_B$ than at $\vec{r}_1$, depending on the topographical overlap of the genuine and best-fitting sources. Indeed, analysis of the ratio

$$\frac{F_1(\vec{r}_B)}{F_1(\vec{r}_1)} \approx \frac{\sqrt{1-b_B(\hat{g}_B^T\hat{g}_1)^2}}{1-a_B(\hat{g}_B^T\hat{g}_1)^2}\,\hat{g}_B^T\hat{g}_1 \tag{10}$$

shows that the common beamformer outputs more signal at the best-fitting source whenever the topographical overlap $\hat{g}_B^T\hat{g}_1$ exceeds a given value, equal to $1/\sqrt{2} \approx 0.7$ at high SNR (where $a_B \approx b_B \approx 1$). The condition $0.7 < \hat{g}_B^T\hat{g}_1 < 1$ defines implicitly a shell where mislocalization must happen.

2.3. Illustration with a toy model simulation

We have demonstrated that the common beamformer is bound to mislocalize the genuine source at $\vec{r}_1$ when the interfering source location $\vec{r}_2$ is within a shell whose shape and size depend on the overlap of their sensor topography and on their SNR. The reason is that the filter weights are tuned to cancel both activities (even though only the genuine source is really active in the considered condition), which leads to a decreased output at the genuine source location $\vec{r}_1$ and increased output somewhere in between $\vec{r}_1$ and $\vec{r}_2$.

We derived this conclusion in the nearby-source limit to reveal the basic mechanism underlying mislocalization of the common beamformer, but the principle extends beyond this approximation. Instead of developing the full analysis (see the supplementary material S1 for explicit expressions), we illustrate this claim using a toy model simulation where an array of sensors placed on a line measures a signal coming from sources underneath that is proportional to the inverse of the squared sensor–source distance. Accordingly, the gain vector for source location $\vec{r} = [x, y]$ at sensors located at $\vec{r}_s = [x_s, 0]$ is $g(\vec{r}) = ||\vec{r} - \vec{r}_s||^{-2}$. We placed 21 sensors with x_s ranging from -10 to $+10$ with spacing of 1 and two sources at $\vec{r}_1 = [-1, -3]$ and $\vec{r}_2 = [1, -3]$, both with an SNR of 30 (i.e., $\alpha_1 = \alpha_2 = 30$). The corresponding sensor profiles are shown in Fig. 1 a. We also depict in Fig. 1 b their weighted combination g_{MAX} pertaining to the common beamformer as well as the source gain g_B at the best-fitting location, which in our case was $\vec{r}_B = [-0.09, -3.34]$ (identified by least-squares minimization of $||\hat{g}(\vec{r}) - \hat{g}_{MAX}||$).

We illustrate the main difference between the standard and common beamformers by considering the filter weights $w_1 = w(\vec{r}_1)$ and $w_B = w(\vec{r}_B)$ (see Figs. 1 c,d). Localization accuracy is assessed in Fig. 2. For the standard beamformer (Fig. 1 c), the weight w_1 follows the sensor profile of the genuine source gain due to the unit-gain constraint, so it exhibits maximum overlap with g_1. The weight w_B tends to follow the profile of g_B to fulfill the unit-gain constraint but is further modified to cancel the genuine source activity at $\vec{r}_1$ in order to minimize the output variance. This leads to poor overlap with g_1. Therefore the point-spread function (4) is maximal at the genuine source location $\vec{r}_1$ with lower values at other locations such as $\vec{r}_B$, and the beamformer localizes accurately (see Fig. 2 a).

We now turn to the common beamformer (Fig. 1 d). Compared to Fig. 1 c, the weight w_1 is modified to enforce the extra activity suppression due to the interfering source, which decreases its overlap with g_1. On the other hand, the weight w_B now follows better the profile of g_B so its overlap with g_1 increases and exceeds that for w_1. The common beamformer thus mislocalizes the genuine source (see Fig. 2 b). It is noteworthy that the fit between w_B and $\hat{g}_B$ was not perfect (Fig. 1 d, compare with the case of w_1 in Fig. 1 c), which reflects the approximate nature of the equivalent beamformer (8). Another deviation from the nearby-source limit is that the best-fitting source and the maximum of the point-spread function are not necessarily located on a line joining $\vec{r}_1$ and $\vec{r}_2$ (Fig. 2 b). Still, the mechanism leading to mislocalization with the common beamformer stands (see also supplementary material S1).

3. Materials and methods

The theoretical developments of Section 2 demonstrate the possibility of mislocalization with the common beamformer. However, these considerations did not quantify to which extent mislocalization happens in the brain, and they were limited to one-dimensional forward-modeling and uncorrelated homogeneous measurement noise. To bypass these limitations, we developed simulations based on two-dimensional forward-modeling derived from anatomical MRIs and MEG noise recordings of 19 subjects. We also considered experimental MEG data acquired in one subject.

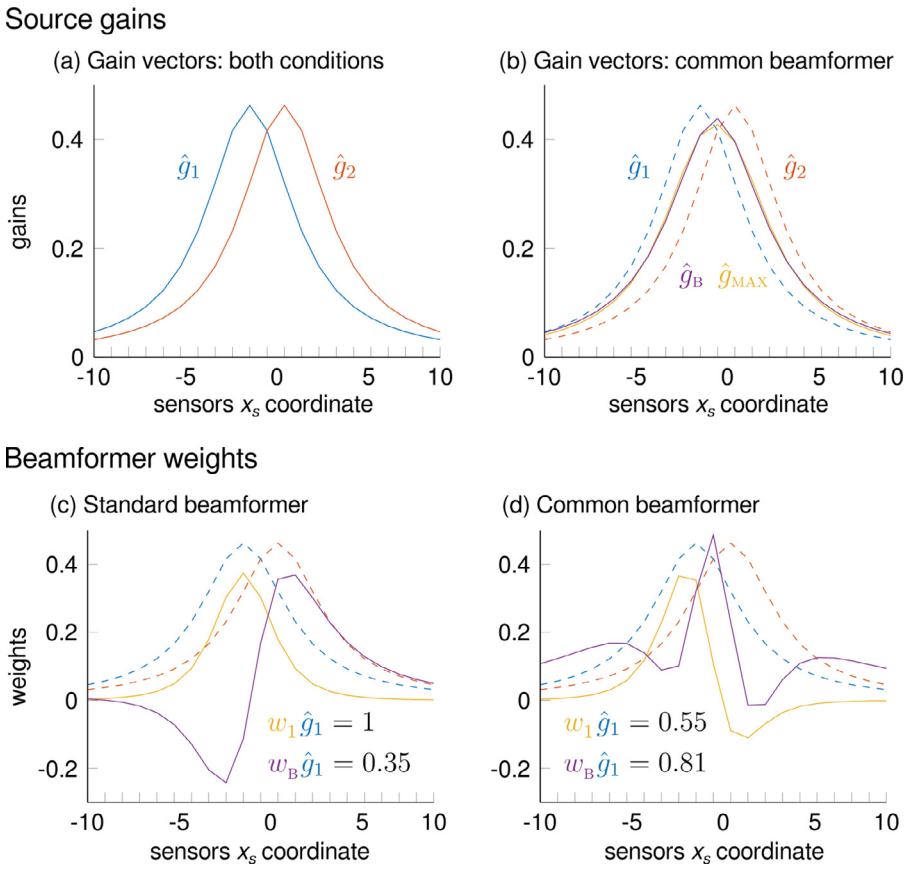

Fig. 1. Standard and common beamformers in the toy model. In this model, a genuine source of standard deviation 1 was placed at $[-1, -3]$ and an interfering source of standard deviation 1 was placed at $[1, -3]$. Sensors located at $[x_s, 0]$ ($x_s = -10, -9, \ldots, 10$) measure a signal equal to the inverse of the squared sensor-source distance. (a) Normalized gain profile corresponding to the genuine ($\hat{g}_1$, blue trace) and interfering ($\hat{g}_2$, red trace) sources. These traces are reproduced in dashed lines in subsequent plots. (b) Sensor profile for which the common beamformer output would be maximum ($\hat{g}_{MAX}$, yellow trace), and its closest (best-fitting) approximation ($\hat{g}_B$, purple trace) that corresponds to a source located at $\vec{r}_B = [-0.09, -3.34]$. (c) Weights for the standard beamformer at $\vec{r}_1$ ($w_1\hat{g}_1 = 1$), while w_B is tuned to cancel the activity coming from $\vec{r}_1$ ($w_B\hat{g}_1 = 0.35$). (d) For the common beamformer, w_1 cancels more of the activity coming from $\vec{r}_1$ ($w_1\hat{g}_1 = 0.55$) than does w_B ($w_B\hat{g}_B = 0.81$).

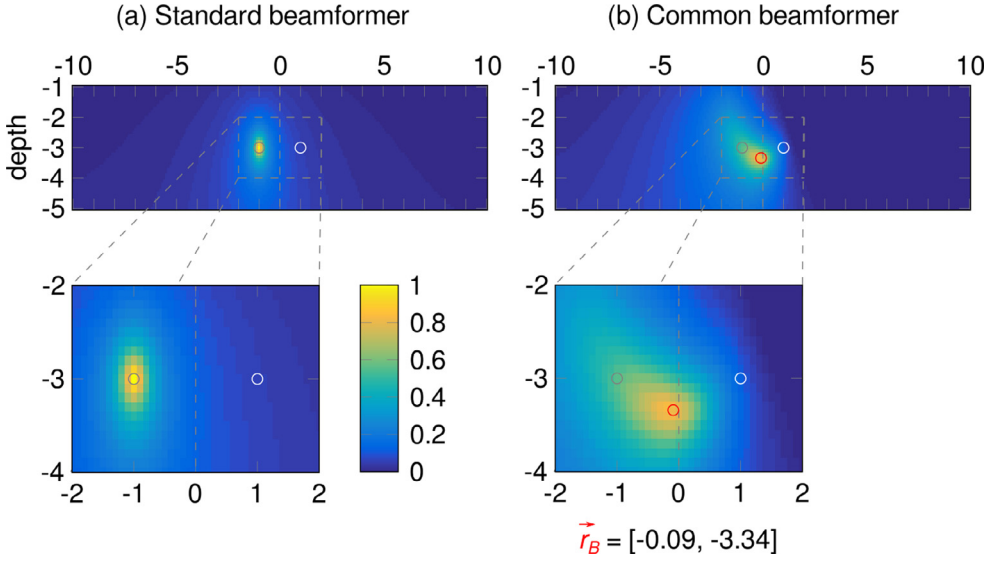

Fig. 2. Point-spread function F_1 for the standard and common beamformers in our toy model, normalized to peak at value 1. The simulated genuine (left grey circle) and interfering (right white circle) sources are shown as well as the best-fitting source location (red circle).

3.1. Subjects

One group of 19 subjects (mean age 30 years, range 23–40 years; 9 females and 10 males; previously included in Vander Ghinst et al., 2016) and a 33-years old male subject participated in this study. All were right-handed according to self-report, and had no history of neuropsychiatric disorder. The study was approved by the ethics committee of CUB Hôpital Erasme. Subjects participated after informed consent.

3.2. Data acquisition

In the group of 19 subjects, five minutes of resting-state MEG data was recorded within a broader experimental protocol (Vander Ghinst et al., 2016). For the single subject, MEG data was recorded while stimulating electrically the left and right tibial nerves. A total of 1200 squared-wave pulses long of 0.2 ms were delivered at weak motor threshold with 500 ms inter-stimulus interval to each side in two separate recordings. All MEG data were collected using a 306-channel whole-scalp neuro-

magnetometer (Vectorview™ for the 19 resting-state data and Triux™ for single-subject data of tibial nerve stimulation, MEGIN Oy, Helsinki, Finland) installed at the CUB Hôpital Erasme and placed in a light-weight magnetically shielded room (Maxshield™, MEGIN Oy, Helsinki Finland) (for its technical characteristics, see Carrette et al., 2011; De Tiège et al., 2008). The recording passband was set to 0.1–330 Hz, and the sampling rate to 1 kHz.

Four head-tracking coils monitored the subjects' head position inside the MEG helmet. Their location relative to anatomical fiducials, as well as at least 150 head-surface points, were recorded prior to MEG data acquisition using an electromagnetic tracker (Fastrack, Polhemus, Colchester, VT, USA). In the group of 19 subjects, electrooculograms (EOG) monitored vertical and horizontal eye movements, and electrocardiogram (ECG) recorded heartbeat signals, time-locked to MEG signals.

High-resolution 3D T1-weighted magnetic resonance images (MRIs) were acquired using a 1.5 Tesla MRI scanner (Intera™, Philips, The Netherlands).

3.3. Data preprocessing

Continuous MEG data was first preprocessed off-line using the temporal signal space separation method (correlation coefficient 0.9; segment length set to recording duration) to suppress external interferences and to correct for head movements (Taulu, Simola, Kajola, 2005). To further suppress heartbeat, eye-blink, and eye-movement artifacts, thirty independent components were then evaluated with the FastICA toolbox (Hyvärinen et al., 2001) from the MEG data low-pass filtered at 25 Hz, and those displaying a correlation exceeding 0.15 with any EOG or ECG signal were subtracted from the full-rank MEG data (Barros et al., 2000). Individual noise covariance matrices (Σ_{NOISE}) were then computed from the cleaned resting-state data restricted to the planar gradiometers. Note that this definition of noise covariance based on resting-state activity marks an important difference with the theoretical analysis of Section 2 based on diagonal, homogeneous noise. The resting state encompasses a complex spatio-temporal source dynamics (see, e.g., Wens et al., 2019), however this dynamics is typically not phase-locked to task-related brain activity. That is why it is usually considered as noise for evoked responses, as will be simulated here.

MEG and MRI coordinate systems were co-registered using the 3 anatomical fiducial points for initial estimation and the head-surface points for further manual refinement. The MRIs were segmented using the Freesurfer software (Reuter et al., 2012). Then, a non-linear transformation from individual MRIs to the MNI brain was computed using the spatial normalization algorithm implemented in Statistical Parametric Mapping (SPM8; see Ashburner and Friston, 1999; Ashburner et al., 1997). This transformation was used to map a homogeneous 5-mm grid sampling the MNI brain volume onto individual brain volumes. For each subject and grid point, the gain matrix corresponding to three orthogonal current dipoles was computed using the one-layer Boundary Element Method implemented in the MNE software suite (Gramfort et al., 2014). This matrix was further reduced to its two first principal components corresponding to the gain of current dipoles approximately tangential to the skull, while the discarded component corresponds to the gain of the close-to-silent current dipole perpendicular to the skull (which would be completely silent in a spherical head model). The resulting two-dimensional gain matrices will be denoted below by

$$G(\vec{r}) = [g_u(\vec{r}), g_v(\vec{r})]\,, \tag{11}$$

where $g_u(\vec{r})$ and $g_v(\vec{r})$ are the gains in the two first principal directions u, v. Note that this source orientation (u, v) plane naturally varies with the corresponding source location $\vec{r}$. This two-dimensional projection is necessary to obtain computationally stable beamformer weights (see Eqs. (13) and (14)).

3.4. Simulated data

As in Section 2, we sought to reconstruct with the common beamformer a genuine source of an evoked response at $\vec{r}_1$ in condition 1, taking into account an interfering source of an evoked response at $\vec{r}_2$ active in a separate condition 2. For the sake of simplicity and computation efficiency, in all simulations, we directly incorporated the effect of simulated sources in the data covariance matrix, rather than actually produce simulated MEG time-series from which covariance matrices would have been derived. The genuine source was placed at the left primary sensory-motor cortex (SM1; MNI coordinates $\vec{r}_1 = [-35, -30, 55]$ mm) along the antero-posterior (y) axis. The corresponding gain vector will be denoted by g_1. The interfering source location $\vec{r}_2$ was probed systematically across the whole brain volume. Its orientation was chosen in its (u, v) plane so that the associated sensor topography maximally overlaps with g_1. Specifically, we chose the combination $g_2 = n_u g_u(\vec{r}_2) + n_v g_v(\vec{r}_2)$ with $n_u^2 + n_v^2 = 1$ that maximizes $\hat{g}_1^{\mathrm{T}} \hat{g}_2$. This setup was chosen based on Section 2 to optimize the detection of possible mislocalization biases and hence represents the worst-case scenario. We do not investigate explicitly the best-case scenario where g_2 is orthogonal to g_1 (which is always achievable by a suitable choice of n_u, n_v) simply because this scenario would systematically lead to no localization error (see Section 2).

In that two-source setting, the data covariance matrix (3) fed to the common beamformer was

$$\Sigma = \frac{1}{2}\sigma_1^2 g_1 g_1^{\mathrm{T}} + \frac{1}{2}\sigma_2^2 g_2 g_2^{\mathrm{T}} + \Sigma_{\text{NOISE}}\,. \tag{12}$$

The main difference with the theoretical considerations of Section 2 is that we used realistic estimates of noise covariance Σ_{NOISE} extracted from individual resting-state data. Given the very large number of time samples in each of these data (of the order of 3×10^5) compared to the number $N = 204$ of sensors, the estimation error on Σ_{NOISE} was negligible. Furthermore, since the same noise covariance estimate was used in the common beamformer and the standard beamformer (obtained with $\Sigma = \sigma_1^2 g_1 g_1^{\mathrm{T}} + \Sigma_{\text{NOISE}}$), the covariance estimation error was preserved and therefore did not hamper their comparison.

We fixed the standard deviation parameters σ_1 and σ_2 in terms of the SNR values (5), using as single-sensor noise level σ_0^2 defined as the mean noise variance across the N sensors (i.e., $\sigma_0^2 = \mathrm{trace}(\Sigma_{\text{NOISE}})/N$). We considered both balanced and unbalanced SNRs across the two conditions, specifically (i) equally high SNRs $\alpha_1 = \alpha_2 = 100$, (ii) equally low SNRs $\alpha_1 = \alpha_2 = 30$, (iii) dominating genuine source $\alpha_1 = 100$, $\alpha_2 = 30$, and (iv) dominating interfering source $\alpha_1 = 30$, $\alpha_2 = 100$. As a comparison, the evoked data for the left and right tibial nerve stimulations had SNR 600 and 400 (see Section 3.7). Lower SNRs $\alpha_1 = \alpha_2 = 10$ are considered in the supplementary material S2.

3.5. Source reconstruction

For source reconstruction, we used the vectorial beamformer with unit-noise-gain constraint, whose two-dimensional weights are obtained as (Sekihara et al., 2001)

$$w_u(\vec{r}) = \frac{\left[(G^{\mathrm{T}}(\vec{r})\Sigma^{-1}G(\vec{r}))^{-1}G(\vec{r})^{\mathrm{T}}\right]_u \Sigma^{-1}}{\sqrt{\Upsilon_{uu}}}\,, \tag{13}$$

and similarly for the other direction v (see Eq. (11)), where the subscript denotes the selection of the corresponding component. The denominator is the square root of the u, u component of the matrix

$$\Upsilon(\vec{r}) = (G^{\mathrm{T}}(\vec{r})\Sigma^{-1}G(\vec{r}))^{-1}(G^{\mathrm{T}}(\vec{r})\Sigma^{-2}G(\vec{r}))(G^{\mathrm{T}}(\vec{r})\Sigma^{-1}G(\vec{r}))^{-1} \tag{14}$$

and ensures a unit-noise normalization $||w_u(\vec{r})|| = 1$. Another weight normalization scheme is considered in the supplementary material S3. The inversion of Σ was stabilized using Tikhonov regularization, i.e., the inverse of each eigenvalue λ was taken as $\lambda/(\lambda^2 + \epsilon^2)$ with the regularization parameter ϵ set to 1% of the largest eigenvalue. (See supplementary material S4 for justification and comparison with another regularization procedure.) Note that the inversion of the 2×2 matrix

$G^{\mathrm{T}}(\vec{r})\Sigma^{-1}G(\vec{r})$ was then well conditioned thanks to the two-dimensional projection described above Eq. (11).

These beamformer weights were used to build the power map in condition 1 as follows (Sekihara and Nagarajan, 2008):

$$P_1(\vec{r}) = \sigma_1^2(w_u(\vec{r})g_1)^2 + \sigma_1^2(w_v(\vec{r})g_1)^2 + w_u(\vec{r})\Sigma_{\mathrm{NOISE}}w_u(\vec{r})^{\mathrm{T}} + w_v(\vec{r})\Sigma_{\mathrm{NOISE}}w_v(\vec{r})^{\mathrm{T}}. \quad (15)$$

This quantity is a two-dimensional, noisy analog to the squared point-spread function $F_1(\vec{r})^2$. It is important to note that, for simplicity, our main simulations used the same gain matrices to generate source activation vectors $g_{1,2}$ (Eqs. (12) and (15)) and to compute the beamformers weights $w_{u,v}(\vec{r})$ (Eqs. (13) and (14)). This corresponds to the so-called "inverse crime" where estimation inaccuracy in gain vectors is not taken into account. The effect of such inaccuracies is explored in the supplementary material S5.

3.6. Mislocalization mapping in simulations

Power maps were computed for each of the 19 subjects and further normalized by their average value for convenience, so that scales are in multiples of the mean power value. We also quantified where and to which extent mislocalization happens. We built a mislocalization map by computing for each possible interfering source the coordinate differences Δx, Δy, and Δz between the locations of the genuine source and of the global maximum of P_1 obtained with the common beamformer. The mislocalization map was then obtained as the Euclidean norm

$$D = \sqrt{\overline{\Delta x}^2 + \overline{\Delta y}^2 + \overline{\Delta z}^2} \quad (16)$$

of these coordinate differences averaged across the 19 subjects.

We also assessed statistically if the resulting mislocalization is higher when using the common beamformer than the standard one. To that aim, we built a statistical map $\chi = \sqrt{Z_x^2 + Z_y^2 + Z_z^2}$, where

$$Z_x = \frac{\overline{\Delta x}_{\mathrm{common}} - \overline{\Delta x}_{\mathrm{standard}}}{\sigma_x + \epsilon_x} \quad (17)$$

is a regularized z score for the mislocalization difference along the x axis, and similarly for Z_y and Z_z. Here, σ_x is the sample standard deviation of this difference, and the regularization parameter ϵ_x was set to 10% of the maximum value of σ_x over all interfering sources, so as to tame the influence of low variance locations (Ridgway et al., 2012). We tested the omnibus null hypothesis that common and standard beamformers produce similar mislocalization errors across all the interfering sources. The statistical threshold for the χ maps at a 5% significance level was obtained from the permutation distribution of the maximum of χ, which was generated by randomly exchanging the beamformer type label ("common" and "standard") for each subject before computing χ (2000 permutations). All supra-threshold values were deemed significant. To further increase the sensitivity of this test while preserving control of the family-wise error rate, we applied the jump-down approach (Nichols and Holmes, 2002). We repeated the same permutation tests restricted to the sub-threshold part of the χ map, determined a new threshold, and retained all supra-threshold sources as being significant. This procedure was continued iteratively until no significant source remained. The resulting set of supra-threshold locations defined a statistical mask that we applied to the mislocalization map D for the common beamformer.

3.7. Comparison of two evoked responses

Lastly, we illustrated the mislocalization effect by applying the common beamformer to experimental MEG data recorded in response to electrical left and right tibial nerve stimulation in one subject. This paradigm was chosen because the recruited brain areas are anatomically close though clearly distinct (i.e., close to the midline within opposite cerebral hemispheres). The preprocessed data was cut into epochs from 100 to 250 ms relative to stimulation onset, and averaged across epochs. (A similar analysis without noise reduction is described in the supplementary material S6.) The covariance matrix Σ was then obtained within time windows of interest on the basis of these epoch-averaged, evoked data. We considered the maximum response times, but also the periods exhibiting maximal correlation between the sensor topographies in the left and right stimulations. This was done to maximize the chance of detecting mislocalization, as the sensor response to a focal brain activation is a proxy of the corresponding source gain, so topographical overlap is maximized in this window (Section 2). Note that we did not include the baseline into the estimation of the covariance matrix, which would have been to the effect of increasing the noise on the covariance matrix and hence decrease the potential for mislocalization.

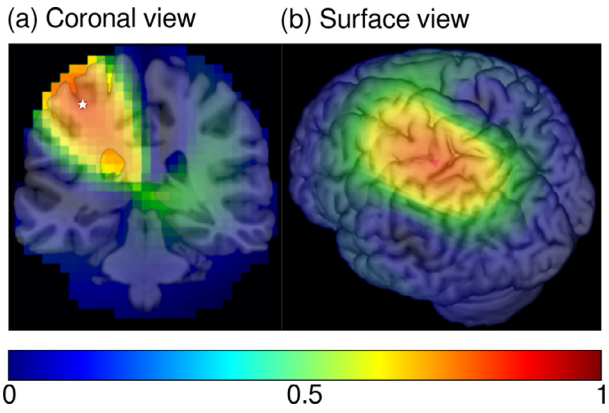

Fig. 3. Example in a typical subject of the topographical overlap between the gain of the genuine source (SM1, white star on left panel) and the maximally-correlated gain at each interfering source. The color scale corresponds to values of overlap $|\cos(\theta_{12})|$.

Power maps in the two conditions (left and right stimulation) were estimated with the weights (13) according to

$$P(\vec{r}) = w_u(\vec{r})\Sigma w_u(\vec{r})^{\mathrm{T}} + w_v(\vec{r})\Sigma w_v(\vec{r})^{\mathrm{T}}. \quad (18)$$

Here Σ denotes either the covariance of the single-condition evoked data within the window of interest (standard beamformer) or their average over the two conditions (common beamformer). Of note, the covariance matrix Σ in Eqs. (13) and (14) was regularized with diagonal loading of 1% of its largest eigenvalue, which was added to its diagonal prior to inversion (see, e.g., Brookes et al., 2008; Gross et al., 2001). This was necessary in the case of these evoked responses, as further justified in the supplementary material S4. We used the bootstrap statistics (200 resamplings) to assess the impact of beamformer type (standard vs. common) on the distance between reconstructed sources to left and right tibial nerve stimulation (Efron and Tibshirani, 1994).

4. Results

Here, we expand our theoretical results using simulated and experimental MEG data. We first examine the spatial structure of source gain overlap, given its importance revealed in Section 2. We then illustrate the mislocalization of the common beamformer using selected power maps and the mislocalization maps obtained from simulations. Finally, we sought to detect mislocalization in MEG evoked responses.

4.1. Topographical overlap of source gains

Fig. 3 presents a map of overlap between the gain vectors of a source placed at the left SM1 cortex and of any other source across the brain volume in the orientation of maximum correlation ($|\cos(\theta_{12})|$ in the notation of Section 2). These maps illustrate that topographical overlap

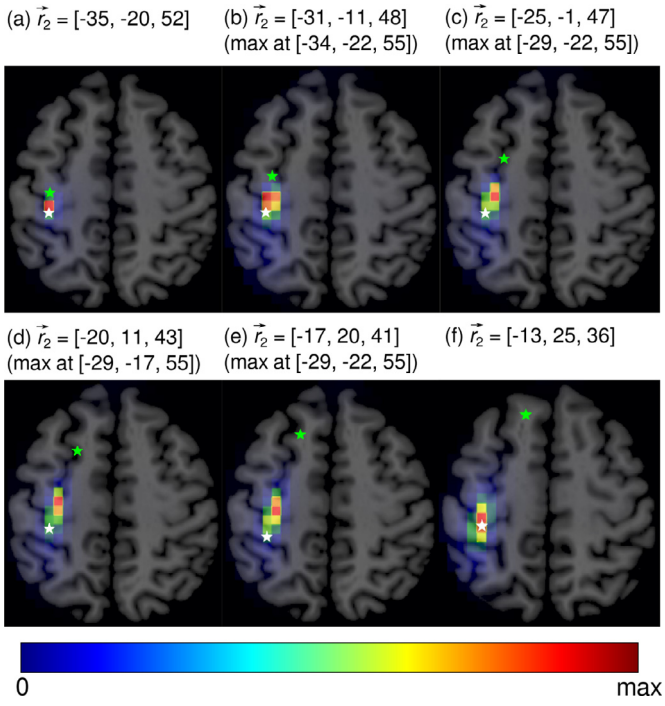

Fig. 4. Example of power maps in a typical subject for the genuine source at left SM1 (white star, $\vec{r}_1 = [-35, -30, 55]$) with $\alpha_1 = 100$ and an interfering source at locations $\vec{r}_2$ (green star) with increasing distances and $\alpha_2 = 100$. Source orientations are optimized for maximum topographical overlap, and locations are given in MNI coordinates (mm). The color scale is from 0 to the map's maximum in each case, to best highlight the maximum's location.

decreases as sources are separated, from complete overlap when they coincide to almost no overlap whatever the source orientation at distances greater than 10 cm. As explained in Section 2, mislocalization is expected for substantial yet non-extreme overlap. Accordingly, Fig. 3 indicates that mislocalization should not occur beyond approximately 5 cm from the genuine source location. Note that this corresponds to a worst-case scenario, as the source gain at the varying location is maximally correlated with the source gain of the left SM1 source, hence maximizing overlap everywhere. This means that this 5 cm domain might be overestimated compared to more realistic situations, where source orientations are not optimized for mislocalization (e.g., anatomically constrained to be normal to the cortical surface).

4.2. Examples of mislocalization bias

Fig. 4 shows the reconstructed power maps in one example subject for the SM1 genuine source and selected interfering sources, both at SNR $\alpha_1 = \alpha_2 = 100$.[2] The global maximum was located in between the genuine source and the interfering source (Fig. 4 a–e). This mislocalization bias was negligible for very close sources (Fig. 4 a), increased as source separation increased (Figs. 4 b–d) to reach 1.4 cm in Fig. 4 d, and then decreased for larger separations down to no mislocalization at inter-source distances larger than 5 cm (Fig. 4 f). These observations fit with our expectations based on Section 2 and Fig. 3.

4.3. Mislocalization maps

Fig. 5 a presents the mislocalization map with balanced SNRs $\alpha_1 = \alpha_2 = 100$ for the same example subject. It shows the magnitude of the localization error (that is, the distance between the global maximum and the genuine source locations) when the interfering source is moved across the brain volume. In accordance with Fig. 4, mislocalization occurred on a shell covering distances from 1 to 5 cm from the genuine source with mislocalization peaking up to 1.6 cm. Note that the absence of mislocalization when genuine and interfering sources almost coincide (as was explained in Section 2) is reflected by a zone of low mislocalization in the close vicinity (say within 1 cm) of the genuine source.

This observation generalized to the group level, as shown in Figs. 5 b,c. The corresponding mislocalization shell was further isolated by the statistical mask exhibiting only the interfering sources yielding mislocalization significantly larger than for the standard beamformer (Fig. 6 a). In this case, the main part of the significant shell was comprised between 1 to 5 cm with mislocalization values mainly between 0.5 and 1 cm (Fig. 6 b). It involved regions where the topographical overlap between genuine and interfering source gains was mainly above 0.6 (Fig. 6 c).

The existence of this mislocalization shell for $\alpha_1 = \alpha_2 = 100$ persisted when we varied the sources SNR. Fig. 6 d illustrates the case of balanced but lower SNR, $\alpha_1 = \alpha_2 = 30$. The corresponding scatter plots indicate an increased size of the significant mislocalization shell as well as higher mislocalization values, generally ranging from 0.5 to 1.5 cm (Fig. 6 e) and topographical overlaps above 0.3 (Fig. 6 f). The case of unbalanced SNRs with dominating interfering source ($\alpha_1 = 30, \alpha_2 = 100$) yielded even greater values of significant mislocalization (Fig. 6 g), reaching up to 2 cm and more (Fig. 6 h) and corresponding topographical overlap mainly above 0.5 (Fig 6 i). The case of unbalanced SNRs with dominant genuine source ($\alpha_1 = 100, \alpha_2 = 30$) led to no significant mislocalization. Further lowering SNRs generally yielded thinner shells of significant mislocalization (see supplementary material S2 for the case $\alpha_1 = \alpha_2 = 10$).

Several variants of these simulation results are reported in the supplementary materials to assess the effect of weight normalization (supplementary material S3), covariance regularization scheme (supplementary material S4) and forward model inaccuracy (supplementary material S5).

4.4. Mislocalization for experimental data

Fig. 7 presents the time courses of the evoked responses to left and right tibial nerve stimulation in our test subject. The gradiometer with maximum absolute amplitude peaked at 44 ms for both the left and right tibial nerve responses, with SNRs of approximately 600 and 400 (respectively). Reconstructions with the common beamformer at these time steps yielded no substantial mislocalization. This is because the left response at 44 ms and the right response at 44 ms (see Figs. 8 a,b) did not overlap sufficiently: their correlation was 0.622. Given the insights of Section 2, this degree of overlap was too low for mislocalization to occur with the common beamformer.

To maximize our chances of disclosing some mislocalization effect, we identified the 10 ms-wide time window exhibiting highest correlation (Figs. 9 and 8 c,d). The resulting window spread from 44 to 54 ms post-stimulus and featured a topographical overlap between 0.656 and 0.800. The corresponding source reconstructions obtained with the standard and common beamformers are displayed in Fig. 10. Peak locations obtained with the standard beamformer (Figs. 10 a,c) located the foot area of the primary somatosensory cortex contralateral to stimulation. They were more than 2.5 cm apart. The common beamformer pulled the two peak locations towards each other (distance reduced to less than 1 cm; Fig. 10 b,d). Bootstrap statistics identified a trend towards significance ($p = 0.095$) for the difference in such distance between standard and common beamformers (i.e., 1.5 cm). This difference in distance is in line with our estimations based on simulations, which yielded mislocalization up to 1 cm (see Fig. 6 b). In the case of right tibial nerve stimulation, the common beamformer even reconstructed the activity in the right (and hence wrong) hemisphere, which is anatomically aberrant.

[2] The sparsity of these maps is likely due to the beamformer's generic properties for good SNRs. Our results however also hold for experimental MEG data (see Section 4.4), where the reconstructed activity maps are smoother.

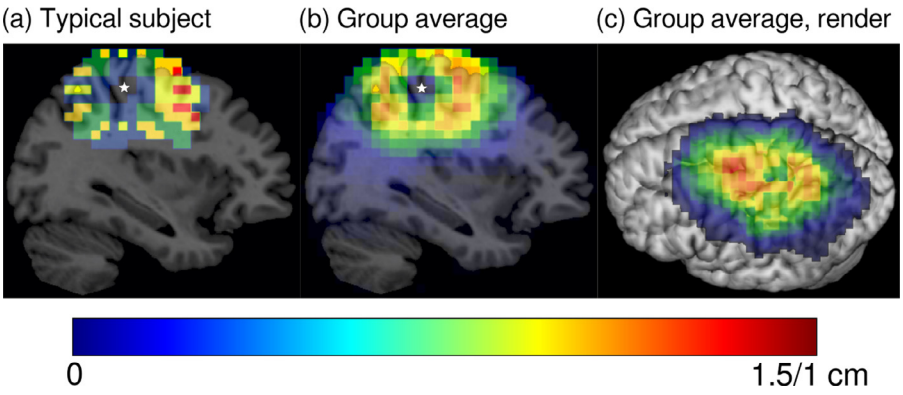

Fig. 5. Mislocalization map in the same example subject as in Fig. 4 (a) (color scale 0–1.5 cm), and group-level mislocalization map (b, c) (color scale 0–1 cm). Genuine source in SM1 with $\alpha_1 = 100$ (white star), and varying interfering source location with $\alpha_2 = 100$. Sagittal slices in the MNI brain are at $x = -35$ mm.

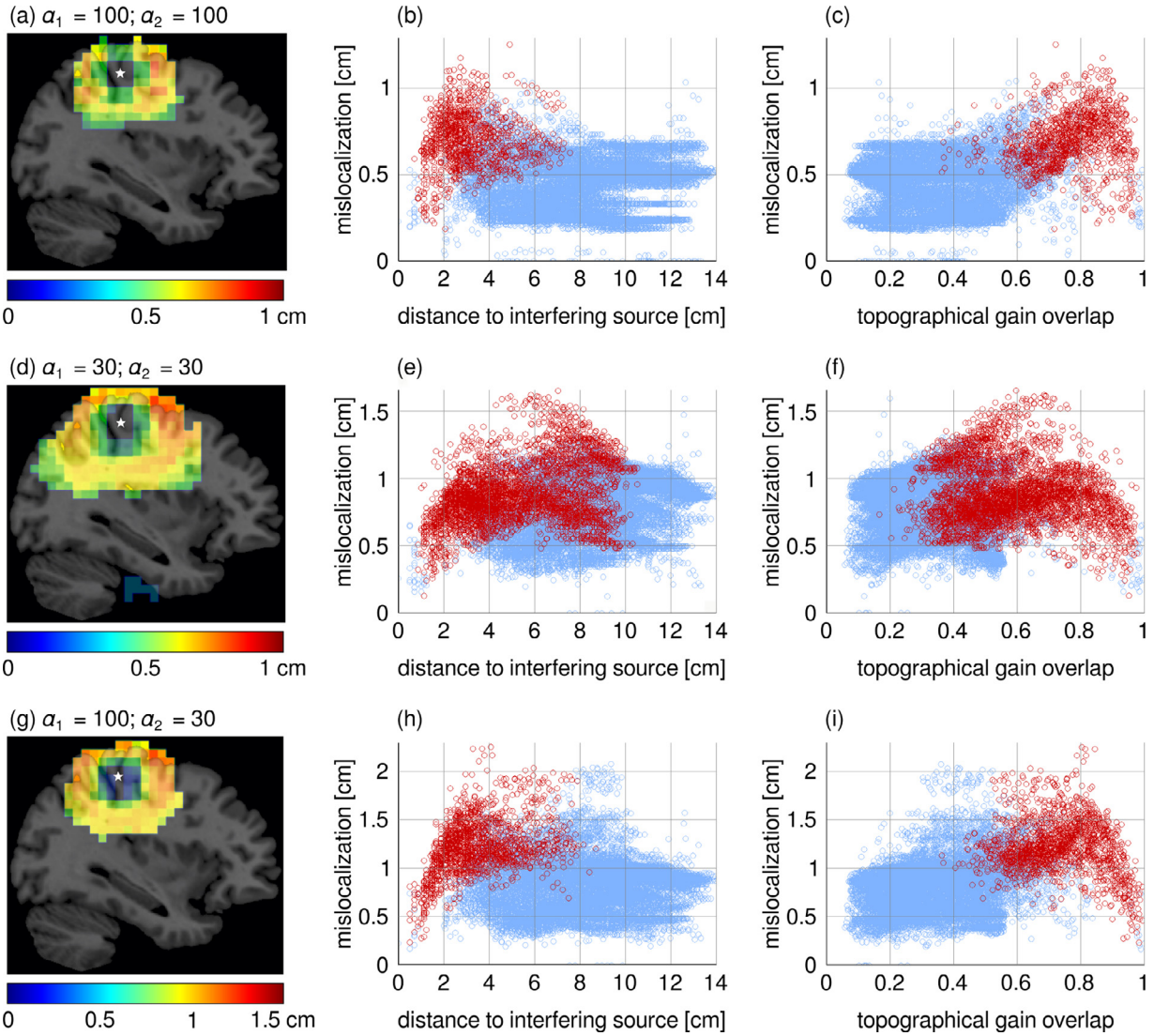

Fig. 6. Mislocalization for the common beamformer compared with the standard one. Only statistically significant values are shown on leftmost maps ($p < 0.05$, permutation test), and they appear in red on the central and rightmost plots depicting the magnitude of mislocalization as a function of the distance to the genuine source (central) or as a function of the topographical overlap between genuine and interfering sources' gain (right). The genuine source is in SM1 (white star on leftmost maps), for different combinations of SNRs.

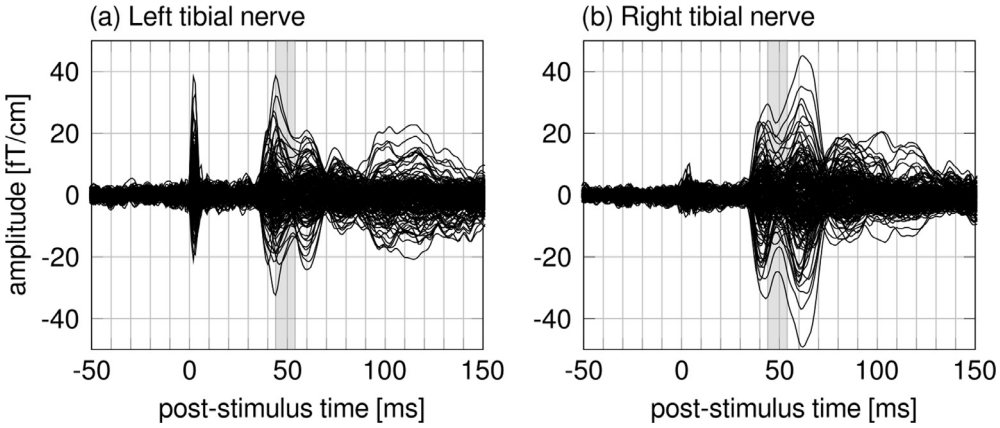

Fig. 7. Evoked responses at all gradiometers to left (a) and right (b) tibial nerve stimulation. The shaded area indicates the window of highest correlation between sensor topographies identified in Fig. 9. Note that the large-amplitude response peaking at 2 3 ms is an artifact caused by the electrical current delivered to the tibial nerve.

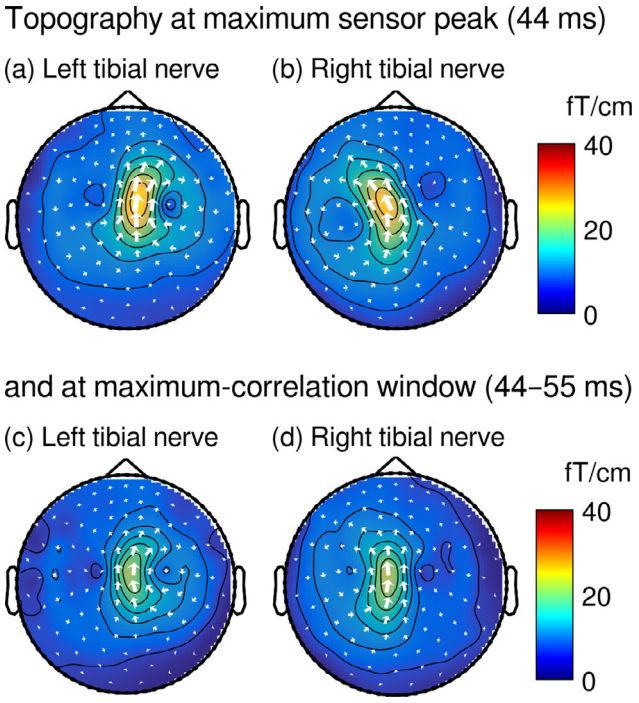

Fig. 8. Topographic distributions of magnetic responses (color scale: Euclidian norm of gradiometer data) for left (a, c) and right (b, d) tibial nerve stimulation at the maximum response (top) or within the maximum correlation window (bottom, see Fig. 9).

Similar results held when analyzing these data without noise suppression (supplementary material S6).

5. Discussion

We have assessed the validity of the recommendation to use a common beamformer when reconstructing MEG sources in more than one condition with the beamformer approach (Gross et al., 2013). Our results demonstrate that such a common beamformer can lead to mislocalization. In the simple setting where there is a single source at different locations in two separate conditions (i.e., in different recordings), the common beamformer reconstructs each source closer to the other than it actually is, hence reducing their differences. This happens when the sources produce sensor responses that overlap substantially yet not completely, which in practice is the case when sources are close to parallel and between 1 and 5 cm apart, although the precise separation actually depends on several parameters such as the SNR in both conditions.

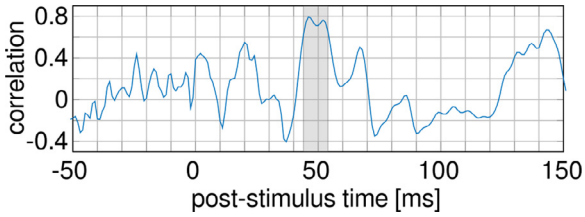

Fig. 9. Correlation between the sensor topographies (gradiometers only) of evoked responses during left and right tibial nerve stimulations as a function of post-stimulus time. A shaded area highlights the window of maximum correlation.

The above conclusions, obtained from analytical considerations and synthetic MEG data simulated with real MEG noise and head models, were in line with experimental MEG data.

5.1. Pitfalls of the common beamformer

In the present report, we have focused on the simple setting in which there is a single "genuine" source in condition 1 and a single "interfering" source in condition 2. We assessed how the reconstruction of the genuine source location with a common beamformer is impacted by the presence of the interfering source. When the interfering source is within 1–5 cm from the genuine source and for a reasonable range of SNRs (30–100), the common beamformer produced a maximum power output somewhere in between the genuine and interfering source locations. In other words, the interfering source acted as an attractor for the reconstructed location of the genuine source.

The mislocalization values obtained in the balanced SNR case were as high as 1.5 cm. Looking at a worst case scenario, for sources 3 cm apart, the common beamformer may reconstruct a single source in the middle, at the same location for both conditions. Along the same lines, in our MEG evoked responses, sources to left and right tibial nerve stimulation were pulled closer to each other by 1.5 cm: initially more than 2.5 cm away, they were reconstructed less than 1 cm apart (Fig. 10). Note that 1–2 cm is about the size of a sulcus.

That said, the amount of mislocalization actually depends on several parameters. Our theory and simulations highlighted the crucial role of source topographical overlap in the generation of mislocalization, so that problems may arise for topographical overlaps exceeding 0.7 (see Section 2.2). Still, the SNR of the genuine and interfering sources do strongly influence this theoretical limit (see Figs. 6 c,f,i). Other details of the beamformer may also matter (e.g., data preprocessing, covariance matrix regularization, or weight normalization). So our estimates provide qualitative rules of thumb but precise evaluations are bound to vary across different implementations. A systematic comparison along the lines of Jaiswal et al. (2020) will be useful in the future.

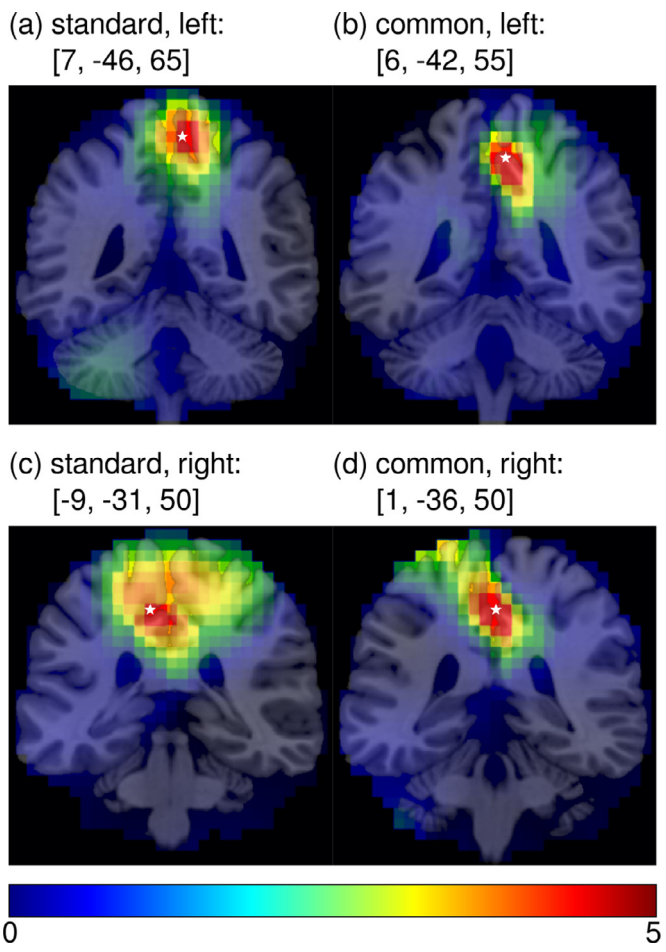

Fig. 10. Reconstructed power maps for left (top) and right (bottom) tibial nerve stimulations with a standard (a, c) and a common (b, d) beamformer. Each map is a temporal average over the maximum-correlation window (see Fig. 9). Color scale from 0 to 5 times the mean power value of each map. MNI coordinates of map maxima reported in mm and indicated on map by a white star.

The first crucial aspect to discuss is topographical overlap. Mislocalization occurs only when genuine and interfering sensor responses do overlap substantially yet not fully. Accordingly, in our simulations we have systematically explored interfering sources whose sensor topography is maximally correlated with that at the genuine location. This means that we have selected sources that are close to parallel. As the angle between sources increases the overlap between sensor responses diminishes, and the mislocalization issue disappears. This effect was also seen in the experimental data. In this case, the overlap varied in time due to a dynamic rotation of the dipolar magnetic field pattern (Fig. 8). Mislocalization was only seen at the time window of maximum correlation between the left and right sensor responses. In this respect, our simulations and experimental data focused on the worst-case scenarios. We did not explore the best-case scenario wherein the interfering source orientation would be selected to generate a sensor topography orthogonal to that of the genuine source simply because this setting would trivially lead to no localization error. Hence, the issue might be less drastic in real applications. For example, beamforming with anatomical constraints (i.e., sources oriented normal to the cortical surfaces) might possibly lead to less amount of mislocalization with the common beamformer.

The second important parameter is source SNR. We have mainly focused on the case of comparable SNRs (exactly equal in the case of our simulations and slightly unbalanced for experimental MEG data). As highlighted above, this very common setting leads to a mislocalization of up to 1.5 cm. It is far from the worst case since unbalanced situations wherein the SNR of the interfering source was about three times that of the genuine source led to larger localization errors of up to 2.3 cm (Fig. 6) and even up to 3 cm in some subjects (not shown). The reconstructed location was pulled all the more towards the interfering location. In the case of experimental MEG data, we indeed observed that the right tibial stimulation, featuring a lower SNR than the left one, was pulled towards the other side of the brain, actually even entering the other hemisphere (Fig. 10 c,d).

Implementational details of the beamformer also affect mislocalization (Jaiswal et al., 2020), though they likely impact the general localization performance of beamformers (including the standard beamformer) rather than being specific to the common beamformer. We found that noise reduction (signal space separation and independent component analysis) does not substantially modulate localization accuracy (supplementary material S6), which makes sense given that beamforming inherently suppresses correlated noise (vanVeen et al., 1997). Although in theory the beamformer actually uses noise to naturally regularize the covariance matrix (vanVeen et al., 1997), avoiding noise reduction does not lift the need of regularization in practical applications such as evoked responses (supplementary material S4). The procedure to regularize the covariance matrix also impacts localization accuracy, and we considered here two widely-used approaches, i.e., Tikhonov and “diagonal loading” regularizations. Significant mislocalization due to the common beamformer was observed with both, although its values were somewhat tamed with the latter (supplementary material S4). Note that “diagonal loading” regularization was used for our experimental MEG data showing mislocalization. Finally, weight normalization also affects localization accuracy. We focused here on the unit-noise-gain beamformer but we also showed that mislocalization remains significant when using the array-gain beamformer, albeit slightly tamed (supplementary material S3).

Lastly, it is worth mentioning that our focus on single-source condition data may not provide fully realistic estimates of the extent of mislocalization with the common beamformer. This simple setting was useful to identify the roots of this mislocalization effect and to systematically investigate the impact of several parameters discussed above. However it may not be representative of more complex experimental situations including several sources per condition. As such, some open questions are how the common beamformer behaves when applied to multi-source configurations and what is the impact of varying the overlap or the SNR of these sources within each condition as well as across the two conditions. Critically, we have not investigated such versatile settings here. Since estimates of localization errors depend on several methodological details, the quantitative results may not be particularly representative anyway. Still, it is reasonable to think that the potential for cancellation and mislocalization is higher because the presence of multiple sources will affect beamformer weights to a higher degree. These questions should be addressed in future studies.

5.2. *Avoiding mislocalization with or without a common beamformer*

In principle, using a common beamformer is safe solely when the sources of the two conditions under study are far from each other or close to orthogonal. Critically, this means that, in several practical situations, the mislocalization that we have exhibited may have a more limited impact than suggested in our simulations (which impose near-parallel orientations). On the other hand, the safe domain of source separation or orientation angle depends among other things on their SNR, so that it may be difficult to be sure *a priori* of the validity of the common beamformer. If a common beamformer must nevertheless be used, a criterion based on values of source gain overlap at both locations could be applied as in Section 4.1, keeping in mind that it can only provide qualitative rules of thumb (as discussed above). Note that the theoretical considerations developed in Section 2 showed that mislocalization happens everywhere except when the genuine and interfering sources

generate perfectly orthogonal sensor responses. Hence in all rigor using the common beamformer exposes one to mislocalization, although in practice the mislocalization biases can be mild and below the spatial resolution of MEG.

The way the covariance matrix is computed can also drastically modulate the potential for mislocalization effect imputable to the common beamformer. There exist different beamforming approaches to source localize evoked responses. The classical approach is the spatiotemporal beamformer where the covariance matrix is that of the epoch-averaged sensor response (Hashimoto et al., 2001; 2003; Sekihara et al., 2001). That approach is well grounded on the theory of adaptive linear filtering and ensures a high localization accuracy (Sekihara and Nagarajan, 2008), but it also requires appropriate regularization to prevent cancellation effects induced by unavoidable deviations from dipolarity in the response, or correlation between multiple sources (Hashimoto et al., 2001; 2003). This type of beamformer is thus susceptible to exhibit the mislocalization of the common beamformer. Of note, our theoretical considerations, simulations and analysis of MEG evoked responses were all developed within that framework. Alternatively, the event-related beamformer rather uses the covariance of the unaveraged data. The resulting filters applied to epoch-averaged data also localizes sources correctly (Sekihara et al., 2001). In this case, the beamformer is tuned to cancel strong electromagnetic interferences such as those produced by heartbeats, eye blinks, tooth braces, cranial clips or implanted stimulators, if those have not been removed with efficient methods such as temporal signal space separation (Bourguignon et al., 2016; Carrette et al., 2011; Kakisaka et al., 2013; Song et al., 2009; Tanaka et al., 2009; Taulu and Hari, 2009; Taulu and Simola, 2006) or independent component analysis (Vigario et al., 2000). This is because unaveraged MEG data is typically dominated by noise and brain rhythms. An important consequence of this observation is that the event-related beamformer does not adapt to the activity of interest during the evoked responses, so that it does not make much of a difference to construct the weights upon the covariance matrix of condition 1, of condition 2 or of their average to reconstruct evoked responses. In other words, the common and the standard beamformers should produce similar results and no mislocalization specific to the common beamformer should arise. Accordingly, this partially non-adaptive character of the weights alleviates the comparability issues raised by Gross et al. (2013). That said, mislocalization of the type reported here could still emerge with the event-related beamformer when dealing with induced responses. In this case, responses in single trials can feature a high SNR of up to 500 at the most responsive sensor (see e.g. Pfurtscheller et al., 1998).

5.3. Conclusion

Altogether, the common beamformer may be a useful tool to identify differences between conditions not ascribable to differences in the filter weights, but the risk of mislocalization exists. Further, the mislocalization effect tends to blur the localization differences between conditions, which is not desirable either. An alternative solution is to use an event-related beamformer built on rest or baseline recordings (Moiseev et al., 2015). One exception, however, could be the case where both conditions exhibit activations of the same focal source but with different SNRs. The common beamformer may then be of use, since it avoids the problem of SNR-dependent spreads (Gross et al., 2013) while avoiding mislocalization (as proven in Section 2).

That said, the very notion of contrasting smooth source maps — regardless of the linear reconstruction method used — is inherently flawed from the beginning (Bourguignon et al., 2018). This is because, as explained for example in Maris and Oostenveld (2007), the size of MEG reconstructions bears no true meaning, and only the location of their maximum (as well as its value) should really be understood as meaningful, at least in the context of focal brain responses.

Based on the above, the only accurate comparison approach that we recommend is to identify maps maxima within each condition and compare statistically their location (Bourguignon et al., 2018) or their amplitude. In this context, the concerns raised in Gross et al. (2013) and the need for a common beamformer are moot. Maps in each condition can be reconstructed with two different methods, the key being to disclose as little mislocalization as possible. Good practice in this endeavor should thus be to use the standard (condition-specific) rather than the common beamformer. Partially non-adaptive methods such as the event-related beamformer or fully non-adaptive approaches such as eLORETA (Pascual-Marqui, 2007), or sparse non-linear algorithms (Friston et al., 2008; Gramfort et al., 2012; 2013; Uutela et al., 1999) are also good candidates.

Author contribution

G.L.G., P.P., V.W. and M.B. designed study; G.L.G., V.W. and M.B. contributed to analytical tools; G.L.G. and M.B. performed experiment; G.L.G., V.W. and M.B. analysed data; G.L.G., P.P., V.W. and M.B. wrote and reviewed manuscript.

Data and code availability statement

The data that support the findings of this study are available from the corresponding author upon reasonable request.

Acknowledgments

G.L.G. was supported by postdoctoral grant from FNRS-FWO Excellence Of Science project Memodyn (ID EOS 30446199). M.B. has been supported by the program Attract of Innoviris (grant 2015-BB2B-10), by the Spanish Ministry of Economy and Competitiveness (grant PSI2016-77175-P), and by the Marie Sklodowska-Curie Action of the European Commission (grant 743562). This study and the MEG project at CUB Hôpital Erasme were financially supported by the Fonds Erasme (Research Convention: “Les Voies du Savoir”, Fonds Erasme, Brussels, Belgium).

Supplementary material

Supplementary material associated with this article can be found, in the online version, at 10.1016/j.neuroimage.2021.117793

References

Ashburner, J., Friston, K., 1999. Nonlinear spatial normalization using basis functions. Hum. Brain Mapp. 7 (4), 254–266.
Ashburner, J., Neelin, P., Collins, D., Evans, A., Friston, K., 1997. Incorporating prior knowledge into image registration. NeuroImage 6 (4), 344–352.
Barros, A.K., Vigario, R., Jousmaki, V., Ohnishi, N., 2000. Extraction of event-related signals from multichannel bioelectrical measurements. IEEE Trans. Biomed. Eng. 47 (5), 583–588.
Bourguignon, M., Molinaro, N., Wens, V., 2018. Contrasting functional imaging parametric maps: The mislocation problem and alternative solutions. NeuroImage 169, 200–211.
Bourguignon, M., Whitmarsh, S., Piitulainen, H., Hari, R., Jousmki, V., Lundqvist, D., 2016. Reliable recording and analysis of meg-based corticokinematic coherence in the presence of strong magnetic artifacts. Clin. Neurophysiol. 127 (2), 1460–1469.
Brookes, M.J., Vrba, J., Robinson, S.E., Stevenson, C.M., Peters, A.M., Barnes, G.R., Hillebrand, A., Morris, P.G., 2008. Optimising experimental design for meg beamformer imaging. NeuroImage 39 (4), 1788–1802.
Carrette, E., De Tiège, X., Op deBeeck, M., Herdt, V.D., Meurs, A., Legros, B., Raedt, R., Deblaere, K., Roost, D.V., Bourguignon, M., Goldman, S., Boon, P., Bogaert, P.V., Vonck, K., 2011. Magnetoencephalography in epilepsy patients carrying a vagus nerve stimulator. Epilepsy Res. 93 (1), 44–52.
Carrette, E., Op de Beeck, M., Bourguignon, M., Boon, P., Vonck, K., Legros, B., Goldman, S., Bogaert, P.V., De Tiège, X., 2011. Recording temporal lobe epileptic activity with meg in a light-weight magnetic shield. Seizure 20 (5), 414–418.
De Tiège, X., Op deBeeck, M., Funke, M., Legros, B., Parkkonen, L., Goldman, S., Bogaert, P.V., 2008. Recording epileptic activity with meg in a light-weight magnetic shield. Epilepsy Res. 82 (2), 227–231.
Efron, B., Tibshirani, R.J., 1994. An Introduction to the Bootstrap. Chapman and Hall/CRC.

Friston, K., Harrison, L., Daunizeau, J., Kiebel, S., Phillips, C., Trujillo-Barreto, N., Henson, R., Flandin, G., Mattout, J., 2008. Multiple sparse priors for the m/eeg inverse problem. NeuroImage 39 (3), 1104–1120.
Gramfort, A., Kowalski, M., Hmlinen, M., 2012. Mixed-norm estimates for the m/EEG inverse problem using accelerated gradient methods. Phys. Med. Biol. 57 (7), 1937–1961.
Gramfort, A., Luessi, M., Larson, E., Engemann, D.A., Strohmeier, D., Brodbeck, C., Parkkonen, L., Hmlinen, M.S., 2014. Mne software for processing meg and eeg data. NeuroImage 86, 446–460.
Gramfort, A., Strohmeier, D., Haueisen, J., Hmlinen, M., Kowalski, M., 2013. Time-frequency mixed-norm estimates: Sparse m/eeg imaging with non-stationary source activations. NeuroImage 70, 410–422.
Greenblatt, R., Ossadtchi, A., Pflieger, M., 2005. Local linear estimators for the bioelectromagnetic inverse problem. IEEE Trans. Signal Process. 53, 3403–3412. 10
Gross, J., Baillet, S., Barnes, G.R., Henson, R.N., Hillebrand, A., Jensen, O., Jerbi, K., Litvak, V., Maess, B., Oostenveld, R., Parkkonen, L., Taylor, J.R., van Wassenhove, V., Wibral, M., Schoffelen, J.M., 2013. Good practice for conducting and reporting meg research. NeuroImage 65, 349–363.
Gross, J., Kujala, J., Hämäläinen, M., Timmermann, L., Schnitzler, A., Salmelin, R., 2001. Dynamic imaging of coherent sources: Studying neural interactions in the human brain. Proc. Natl. Acad. Sci. 98 (2), 694–699.
Hämäläinen, M., Hari, R., Ilmoniemi, R.J., Knuutila, J., Lounasmaa, O.V., 1993. Magnetoencephalography—theory, instrumentation, and applications to noninvasive studies of the working human brain. Rev. Mod. Phys. 65, 413–497.
Hari, R., Puce, A., 2017. MEG-EEG primer. Oxford University Press, Oxford, New York.
Hashimoto, I., Kimura, T., Iguchi, Y., Takino, R., Sekihara, K., 2001. Dynamic activation of distinct cytoarchitectonic areas of the human si cortex after median nerve stimulation. Neuroreport 12, 1891–1897. 08
Hashimoto, I., Kimura, T., Tanosaki, M., Iguchi, Y., Sekihara, K., 2003. Muscle afferent inputs from the hand activate human cerebellum sequentially through parallel and climbing fiber systems. Clin. Neurophysiol. 114 (11), 2107–2117.
Hillebrand, A., Singh, K.D., Holliday, I.E., Fopturlong, P.L., Barnes, G.R., 2005. A new approach to neuroimaging with magnetoencephalography. Hum. Brain Mapp. 25 (2), 199–211.
Hyvärinen, A., Karhunen, J., Oja, E., 2001. Independent Component Analysis. John Wiley & Sons.
Jaiswal, A., Nenonen, J., Stenroos, M., Gramfort, A., Dalal, S.S., Westner, B.U., Litvak, V., Mosher, J.C., Schoffelen, J.-M., Witton, C., Oostenveld, R., Parkkonen, L., 2020. Comparison of beamformer implementations for meg source localization. NeuroImage 216, 116797.
Kakisaka, Y., Mosher, J.C., Wang, Z.I., Jin, K., Dubarry, A.-S., Alexopoulos, A.V., Burgess, R.C., 2013. Utility of temporally-extended signal space separation algorithm for magnetic noise from vagal nerve stimulators. Clin. Neurophysiol. 124 (7), 1277–1282.
Maris, E., Oostenveld, R., 2007. Nonparametric statistical testing of eeg- and meg-data. J. Neurosci. Methods 164 (1), 177–190.
Moiseev, A., Doesburg, S.M., Grunau, R.E., Ribary, U., 2015. Minimum variance beamformer weights revisited. NeuroImage 120, 201–213.
Nichols, T.E., Holmes, A.P., 2002. Nonparametric permutation tests for functional neuroimaging: a primer with examples. Hum. Brain Mapp. 15 (1), 1–25.
Wens, V., Bourguignon, M., Vander Ghinst, M., Mary, A., Marty, B., Coquelet, N., Naeije, G., Peigneux, P., Goldman, S., De Tiège, X., 2019. Synchrony, metastability, dynamic integration, and competition in the spontaneous functional connectivity of the human brain. NeuroImage 199, 313–324.
Pascual-Marqui, R. D., 2007. Discrete, 3d distributed, linear imaging methods of electric neuronal activity. part 1: exact, zero error localization. ArXiv e-prints, arXiv:0710.3341.
Pfurtscheller, G., Zalaudek, K., Neuper, C., 1998. Event-related beta synchronization after wrist, finger and thumb movement. Electroencephalogr. Clin. Neurophysiol./Electromyogr. Motor Control 109 (2), 154–160.
Reuter, M., Schmansky, N.J., Rosas, H.D., Fischl, B., 2012. Within-subject template estimation for unbiased longitudinal image analysis. NeuroImage 61 (4), 1402–1418.
Ridgway, G.R., Litvak, V., Flandin, G., Friston, K.J., Penny, W.D., 2012. The problem of low variance voxels in statistical parametric mapping; a new hat avoids a haircut. NeuroImage 59 (3), 2131–2141.
Robinson, S., 1999. Functional neuroimaging by synthetic aperture magnetometry (sam). Recent advances in biomagnetism.
Sekihara, K., Nagarajan, S., 2008. Adaptive spatial filters for electromagnetic brain imaging. Ser. Biomed. Eng..
Sekihara, K., Nagarajan, S.S., Poeppel, D., Marantz, A., Miyashita, Y., 2001. Reconstructing spatio-temporal activities of neural sources using an meg vector beamformer technique. IEEE Trans. Biomed. Eng. 48 (7), 760–771.
Song, T., Cui, L., Gaa, K., Feffer, L., Taulu, S., Lee, R.R., Huang, M., 2009. Signal space separation algorithm and its application on suppressing artifacts caused by vagus nerve stimulation for magnetoencephalography recordings. J. Clin. Neurophysiol. 26 (6), 392–400.
Tanaka, N., Thiele, E.A., Madsen, J.R., Bourgeois, B.F., Stufflebeam, S.M., 2009. Magnetoencephalographic analysis in patients with vagus nerve stimulator. Pediatr. Neurol.y 41 (5), 383–387.
Taulu, S., Hari, R., 2009. Removal of magnetoencephalographic artifacts with temporal signal-space separation: demonstration with single-trial auditory-evoked responses. Hum. Brain Mapp. 30 (5), 1524–1534.
Taulu, S., Simola, J., 2006. Spatiotemporal signal space separation method for rejecting nearby interference in MEG measurements. Phys. Med. Biol. 51 (7), 1759–1768.
Taulu, S., Simola, J., Kajola, M., 2005. Applications of the signal space separation method. IEEE Trans. Signal Process. 53 (9), 3359–3372.
Uutela, K., Hmlinen, M., Somersalo, E., 1999. Visualization of magnetoencephalographic data using minimum current estimates. NeuroImage 10 (2), 173–180.
Vander Ghinst, M., Bourguignon, M., Op de Beeck, M., Wens, V., Marty, B., Hassid, S., Choufani, G., Jousmki, V., Hari, R., Van Bogaert, P., Goldman, S., De Tiège, X., 2016. Left superior temporal gyrus is coupled to attended speech in a cocktail-party auditory scene. J. Neurosci. 36 (5), 1596–1606.
vanVeen, B.D., vanDrongelen, W., Yuchtman, M., Suzuki, A., 1997. Localization of brain electrical activity via linearly constrained minimum variance spatial filtering. IEEE Trans. Biomed. Eng. 44, 867–880.
Vigario, R., Sarela, J., Jousmiki, V., Hamalainen, M., Oja, E., 2000. Independent component approach to the analysis of eeg and meg recordings. IEEE Trans. Biomed. Eng. 47 (5), 589–593.